



Publication Year	2022
Acceptance in OA @INAF	2022-03-17T14:00:49Z
Title	Extreme-ultraviolet- and X-Ray-driven Photochemistry of Gaseous Exoplanets
Authors	Locci, Daniele; PETRALIA, Antonino; MICELA, Giuseppina; MAGGIO, Antonio; CIARAVELLA, Angela; et al.
DOI	10.3847/PSJ/ac3f3c
Handle	http://hdl.handle.net/20.500.12386/31667
Journal	THE PLANETARY SCIENCE JOURNAL
Number	3



Extreme-ultraviolet- and X-Ray-driven Photochemistry of Gaseous Exoplanets

Daniele Locci , Antonino Petralia , Giuseppina Micela , Antonio Maggio , Angela Ciaravella , and Cesare Cecchi-Pestellini

INAF—Osservatorio Astronomico di Palermo, P.za Parlamento 1, I-90134 Palermo, Italy; cesare.cecchipestellini@inaf.it

Received 2021 August 18; revised 2021 November 2; accepted 2021 November 30; published 2022 January 11

Abstract

The interaction of exoplanets with their host stars causes a vast diversity in bulk and atmospheric compositions and physical and chemical conditions. Stellar radiation, especially at the shorter wavelengths, drives the chemistry in the upper atmospheric layers of close orbiting gaseous giants, providing drastic departures from equilibrium. In this study, we aim at unfolding the effects caused by photons in different spectral bands on the atmospheric chemistry. This task is particularly difficult because the characteristics of chemical evolution emerge from many feedbacks on a wide range of timescales, and because of the existing correlations among different portions of the stellar spectrum. In describing the chemistry, we have placed particular emphasis on the molecular synthesis induced by X-rays. The weak X-ray photoabsorption cross sections of the atmospheric constituents boost the gas ionization to pressures inaccessible to vacuum and extreme-ultraviolet photons. Although X-rays interact preferentially with metals, they produce a secondary electron cascade able to ionize efficiently hydrogen- and helium-bearing species, giving rise to a distinctive chemistry.

Unified Astronomy Thesaurus concepts: [Exoplanet atmospheric composition \(2021\)](#)

1. Introduction

Exoplanets form and evolve under the influence of their host stars. In the process, planetary atmospheres naturally arise and modify under selective environmental constraints, providing an astonishing diversity in compositions and physical and chemical conditions. Our knowledge of exoplanets' atmospheres has improved dramatically over the past two decades (e.g., Tsiaras et al. 2019; Jacobbe et al. 2021), spanning a broad range of planetary types, comprising also gas and ice giants and super-Earths. Just as it occurred for solar system planets, an esoteric field of research is now becoming a major area of interest to physicists and chemists.

Theoretical models are beginning to yield important insights into the chemistry of exoplanetary atmospheres (e.g., Venot & Agúndez 2015). While the chemical composition is at the equilibrium in deep atmospheric layers (Madhusudhan et al. 2016), kinetic processes drive drastic departures from equilibrium in the upper regions of an atmosphere and may also involve the possibility of escape of its constituents to space (e.g., Koskinen et al. 2014; King et al. 2018). The main kinetic mechanisms affecting equilibrium chemistry are transport-induced quenching and photochemistry. Here we use the term photochemistry in a broad sense, including the effects of ionizing radiation (usually called radiation chemistry). Photochemical reactions dominate in the upper atmospheric layers, in a range of pressure determined by the composition and the stellar illumination.

In this work, we are mainly interested in the effects of the stellar high-energy radiation on the upper atmospheric layers of gaseous giants, occurring for pressures lower than $P \sim 10^{-2}$ – 10^{-3} bars. Some previous studies investigate the impact of molecular photodissociation on chemical abundances

(e.g., Moses et al. 2011; Molaverdikhani et al. 2019), while others include the effects of photoionization processes and ion-neutral chemistry (e.g., García Muñoz 2007; Erkaev et al. 2013; Bourgalais et al. 2020), although in such a context just a few contain extended chemical networks (e.g., Barth et al. 2021). Not many works include detailed descriptions of the secondary electron cascade (e.g., Cecchi-Pestellini et al. 2006; Shematovich et al. 2014). Additional ionizing sources, such as cosmic rays and stellar energetic particles, are addressed in Airapetian et al. (2016, 2017) and Barth et al. (2021), while lightning and charge processes are discussed in Helling & Rimmer (2019).

A key element in the accurate description of photochemistry is the representation of the illuminating radiation field and its energy dependence, including the energy tail extended into the X-ray domain. Stellar radiation may present correlations among the intensities in various spectral ranges (e.g., Sanz-Forcada et al. 2011; King et al. 2018) and significant variations with the stellar age impacting differently at different energies (Micela 2002; Ribas et al. 2005). Thus, the wide dispersion in radiation fields adopted in the literature is not surprising, either in spectral ranges or in shapes. Some authors assume observed spectra of specific stars, e.g., using Hubble Space Telescope and XMM-Newton/Swift telescope (Barth et al. 2021), or the PHOENIX library (e.g., Kitzmann et al. 2018); others scale the solar spectrum by means of coronal models (e.g., Sanz-Forcada et al. 2011), as done by Chadney et al. (2015), or exploit spectra taken from the Virtual Planetary Laboratory, to investigate the effect of an increased stellar activity (Shulyak et al. 2020). Stellar X-ray emission may also be simulated through thermal bremsstrahlung (Lorenzani & Palla 2001) and thermal emission of hot plasmas (e.g., Cecchi-Pestellini et al. 2009; Locci et al. 2018).

Because of their high energies, extreme-ultraviolet (EUV) and X-ray photons produce phenomena that cannot be caused in any other of the lower-energy bands, regardless of their larger fluxes. In atmospheres with solar-like composition, the main interactions of EUV photons occur in the very upper



Original content from this work may be used under the terms of the [Creative Commons Attribution 4.0 licence](#). Any further distribution of this work must maintain attribution to the author(s) and the title of the work, journal citation and DOI.

Table 1
Chemical Species

Atoms	Species
H, He	H, He, H ₂
H, O	O, O(1D), O ₂ , O ₃ , OH, H ₂ O, HO ₂ , H ₂ O ₂
H, O, C	C, C ₂ , CH, CH ₂ , CH ₃ , CH ₄ , C ₂ H ₂ , C ₂ H, C ₂ H ₃ , C ₂ H ₄ , C ₂ H ₅ , C ₂ H ₆ , HCO, CO, CO ₂ , H ₂ CO, C ₂ HO, CH ₃ O, CH ₃ O ₂ , CHO ₂ , CH ₂ O ₂ , CH ₄ O ₂ , CH ₂ OH, CH ₃ OH, C ₂ H ₃ O, C ₂ H ₂ O, C ₂ H ₄ O, C ₂ H ₅ O
H, O, C, N	N, N ₂ , NH, NH ₂ , NH ₃ , N ₂ H ₃ , N ₂ H ₄ , NO, N ₂ O, NO ₂ , NO ₃ , N ₂ O ₅ , HNO, HNO ₂ , HNO ₃ , HCN, CN, CNO, HCNO, HNCO, HCONH ₂ , CH ₃ N, C ₂ H ₂ N
Additional ions	H ₃ ⁺ , HeH ⁺ , H ₃ O ⁺

layers, while X-rays, due to their smaller absorption cross sections, may penetrate much further downward. A unique feature of ionizing radiation is that all the relevant processes are dominated by a secondary, low-energy electron cascade generated by the primary photoelectron (Maloney et al. 1996; Arumainayagam et al. 2021). The effects produced by secondary electrons are by far more important than the corresponding ionization, excitation, and dissociation events caused directly by X-rays (e.g., Locci et al. 2018). This is a consequence of the large primary photoelectron energies. Such secondary cascade keeps ionizing the gas (Cecchi-Pestellini et al. 2006; Johnstone et al. 2018). At the end of the energy degradation process, the residual energy incapable of providing further excitation goes into the gas heating (Dalgarno et al. 1999; Cecchi-Pestellini et al. 2006). The global chemical effect is a substantial rise in the ionization level, extending deeply into the atmosphere. When the electron fraction in the gas exceeds a few percent, electrons preferentially lose their energies through electron–electron Coulomb interactions (Dalgarno et al. 1999), so that too-large radiation fluxes produce rather weak nonthermal effects.

In Section 2 we describe the model and the data needed to describe specific representations. In Section 3 we present the results for a model defined by standard assumptions in the main physical and chemical parameters (e.g., X-ray luminosity and metallicity), and we compare them to those stemming from variations in such fiducial values. In Section 4 we discuss the results and outline our conclusions.

2. Chemistry and Radiation

We have developed a one-dimensional thermochemical and photochemical kinetics model to describe the vertical chemical profiles of 128 selected species, including electrons (see Table 1). All the neutral species listed in the table possess singly charged, positive counterparts. No anions are included in the network. The selected species consist of five elements—H, He, C, N, and O—coupled through a network of 1978 chemical reactions. The reaction inventory contains bimolecular, termolecular, thermodissociative, ion–neutral, and photochemical reactions. The latter include photodissociations, mainly due to UV and EUV radiation, and photoionizations by EUV radiation and X-rays. Specifically, we consider 617 neutral–neutral reactions and 912 neutral–ion reactions for a total of 1529 bimolecular reactions, 40 termolecular reactions, 70 thermodissociative reactions, and 127 photochemical reactions including either dissociation or ionization processes; 212 neutral–neutral and termolecular reactions have been reversed. The list of reactions is reported in the Supplementary Materials available at <https://doi.org/10.5281/zenodo.5638699>.

The chemical evolution is described by the system of differential equations

$$\frac{dn_i}{dt} = P_i - n_i L_i, \quad (1)$$

where n_i is the number density of the i th species and P and L are production and destruction terms referring to all chemical and physical processes that produce and destroy the i th species. They are therefore functions of all the species included in the network of chemical reactions. The time derivative is to be understood as comoving. Although the density-based solver may be coupled to flow and energy equations, we do not consider any motion within the fluid, with the chemistry evolving in a static atmosphere. While vertical mixing (and other motions) may indeed be important in the chemical balance of planetary atmospheres (e.g., Moses et al. 2011; Agúndez et al. 2014), we choose not to include atmospheric dynamics (and, in general, any form of nonchemical perturbation), to highlight the role of dissociating and ionizing radiation as a source of chemical disequilibrium, and primarily the relative importance of different spectral energy bands.

2.1. Photochemistry

Photochemical rates describing both dissociation and ionization are computed as follows:

$$\beta(r) = \int_{E_{\text{th}}}^{\infty} \sigma(E) F(E, r) dE, \quad (2)$$

where $\sigma(E)$ is the cross section associated with a specific photoprocess, E_{th} is the corresponding energy threshold, and $F(E, r)$ is the radiative flux at the altitude r in the atmosphere. Ionizations must be supplemented by an additional term including the effects of the secondary electron cascade

$$\beta_{\text{sec}} = \int n_{\text{sec}}(E) v(E) \sigma_e(E) dE \quad (3)$$

(e.g., Ádámkóvics et al. 2011; Locci et al. 2018), where $v(E)$ is the electron velocity, $n_{\text{sec}}(E)$ is the absolute number distribution of secondary electrons, and $\sigma_e(E)$ is the energy-dependent electron impact ionization cross section. Typically, such cross sections have an asymmetric bell shape, with a threshold around 10 eV and a peak at 100–300 eV, while declining to small values around 1 keV (e.g., Hudson et al. 2004). Equation (3) includes also the contribution of Auger electrons (see Locci et al. 2018). The number distribution of secondary electrons depends on the inverse of the mean energy per ion pair W (e.g., Cecchi-Pestellini & Aiello 1992), which is the initial energy of the photoelectron divided by the number of

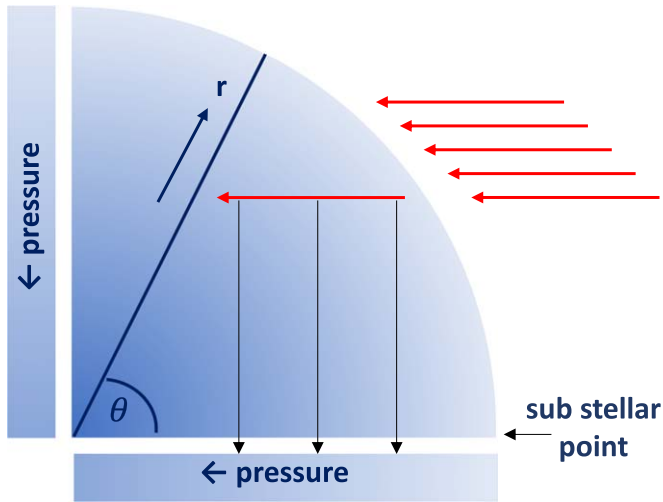


Figure 1. The geometry of the radiation transfer in our model, with the incoming radiation traveling horizontally. The zenith angle θ identifies the radial path along which the chemistry is computed. The vertical black arrows indicate the pressures sampled along the photon path.

secondary ionizations produced as the particle comes to rest. In a gas of solar-like composition, the limiting value of W at high energies is ~ 35 eV, while it is infinite at the ionization threshold (Dalgarno et al. 1999). For this reason, the contribution of the secondary electron cascade decreases sharply when the energy approaches the Lyman continuum. We compute W as a function of the energy of the primary photoelectron, for different abundance ratios and electronic concentrations as done in Cecchi-Pestellini et al. (2006), and store them in a look-up table.

We use measured or calculated photoabsorption cross sections (see, e.g., the online database Photoionization/Dissociation Rates;¹ Huebner & Mukherjee 2015). In those cases where data were not available, we approximate molecular X-ray absorption cross sections by means of the cross sections of the constituent atoms (Maloney et al. 1996; Yan & Dalgarno 1997). The individual atomic cross sections are taken from the compilation of Verner et al. (1996). Known total cross sections provide support to such an assumption. Photodestruction cross sections in lower-energy spectral ranges have been taken from existing compilations (e.g., KIDA, the Kinetic Database for Astrochemistry; Wakelam et al. 2015).

2.2. Radiative Transfer

We consider a one-dimensional geometry, in which a stratified, cloud-free atmosphere is illuminated by a stellar photon flux in the range between 3 and 10,000 eV, and we derive the chemistry along a direction defined by the zenith angle θ (Figure 1).

The radiation at any altitude r is obtained as

$$F(E, r) = F_{\star}(E)e^{-\tau(E,r)}, \quad (4)$$

where $F_{\star}(E)$ is the stellar flux impinging at the (arbitrary) outer boundary of the atmosphere and $\tau(E, r)$ is the total atmospheric

optical depth at the altitude r ,

$$\tau(E, r) = \sum_i \sigma_i(E)N_i(r). \quad (5)$$

In Equation (5), $\sigma_i(E)$ and $N_i(r)$ are the total absorption cross section and the column density of the i th species, respectively; the latter depends on the zenith angle, and it is obtained by integrating along the horizontal direction identified by the corresponding radiation path, as illustrated in Figure 1.

2.3. Input Values and Boundary Conditions

We assume a planet with mass equal to half the Jupiter mass, orbiting around a Sun-like star with solar bolometric luminosity. The adopted stellar spectrum is a mosaic from several sources. Low-energy wave bands, up to the Lyman continuum, are described by a PHOENIX library model of a G-type star (Husser et al. 2013), plus an Ly α emission line, whose intensity is related to the X-ray luminosity (Linsky et al. 2020). The spectral luminosity ($\text{erg s}^{-1} \text{eV}^{-1}$) in the X-ray domain (0.1–10 keV), \mathcal{L}_X , is modeled exploiting Raymond–Smith models for the thermal emission of hot plasmas (Raymond & Smith 1977). The total X-ray luminosity (in erg s^{-1}),

$$L_X = \int_{0.1 \text{ keV}}^{10 \text{ keV}} \mathcal{L}_X(E, T_X) dE, \quad (6)$$

and the hardness of the spectrum (i.e., its temperature, T_X) are free parameters.

EUV radiation (13.6–100 eV) is difficult to determine observationally, and its quantification is frequently based on semiempirical models extended into the EUV domain from either X-ray or UV observations (e.g., Chadney et al. 2015; Fontenla et al. 2015). This can be done by reconstructing the EUV emission from Ly α measurements (Linsky et al. 2014), or through solar data from the TIMED/SEE mission (Chadney et al. 2015), extrapolating them to XMM-Newton and Chandra observations (King et al. 2018). We follow the approach put forward by Sanz-Forcada et al. (2011), who derived an expression relating the EUV and X-ray luminosities, based on synthetic coronal models for a sample of main-sequence stars. Since in the EUV energy range the spectral shape is rather uncertain, we adopt a flat spectral distribution.

Ultimately, we adopt (1) a hot plasma thermal emission for photon energies between 1 keV and 100 eV (X-rays), with the integrated luminosity, Equation (6), and the plasma temperature, T_X , being free parameters; (2) a constant spectrum (not dependent on photon energy) in the EUV band $100 \text{ eV} < E < 13.6 \text{ eV}$, whose luminosity scales directly with the X-ray luminosity according to the Sanz-Forcada et al. (2011) relation, $L_{\text{EUV}} = 6.31 \times 10^4 L_X^{0.86}$; (3) an Ly α profile at 10.2 eV, whose intensity is related to the X-ray luminosity by the expression $L_{\text{Ly}\alpha} = 4.57 \times 10^{16} L_X^{0.43}$ derived from data reported in Linsky et al. (2020); and (4) a PHOENIX G-type star model providing the flux in the UV spectral range between 3 and 13.6 eV. This last portion of the stellar emission is the only one depending on the star spectral type. In Figure 2, we report the adopted illuminating radiation field, under some assumptions on the brightness and hardness of the X-ray component.

The temperature profile is not calculated self-consistently within the code. We assume an isothermal atmosphere, where the chosen value is a free parameter (e.g., the planetary

¹ <https://phidrates.space.swri.edu>

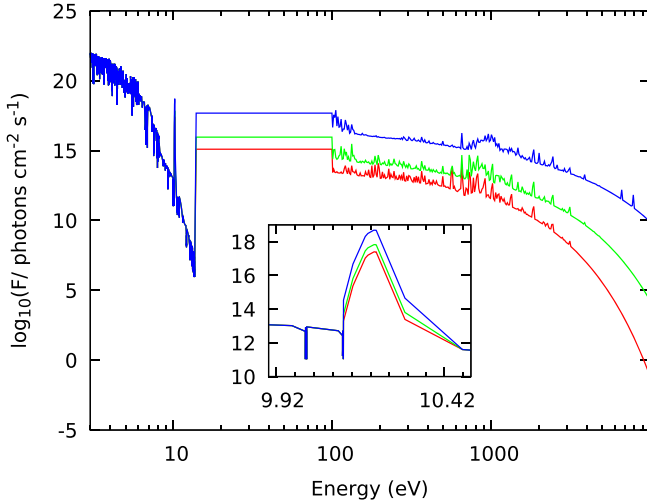


Figure 2. Stellar emission F in the energy range between 3 eV and 10 keV. Red line: $L_X = 1 \times 10^{27}$ erg s $^{-1}$, $T_X = 0.3$ keV; green line: $L_X = 1 \times 10^{28}$ erg s $^{-1}$, $T_X = 0.5$ keV; blue line: $L_X = 1 \times 10^{30}$ erg s $^{-1}$, $T_X = 1$ keV. In the EUV band, we assume a flat spectral shape related to the X-ray luminosity by the Sanz-Forcada et al. (2011) relation. In the inset, we report the portion encompassing the Ly α line, which is also related to L_X (Linsky et al. 2020); the asymmetry in the line profile stems out of the resolution with which we sample the spectrum.

equilibrium temperature). While X-rays may give an important contribution to the heating of hydrogen-rich planetary atmospheres (e.g., Cecchi-Pestellini et al. 2009), we make such an assumption, to avoid that temperature variations can influence and entangle the impact of different spectral bands on the chemical profiles. We consider a range in pressure extending from $P = 1 \times 10^3$ bars to 1×10^{-11} bars. For each pair of values P – T , the remaining derived atmospheric variables, e.g., density and altitude, are obtained by imposing hydrostatic equilibrium.

We assume a solar chemical composition, with concentrations taken from the compilation of Asplund et al. (2009). As initial conditions, we take the gas in each layer to be neutral and in atomic form. In Figure 3, we report the total photoionization cross section, computed considering all the elements present in the atmospheric gas in either neutral or singly ionized atomic forms. This quantity is close to the photoabsorption cross section in the upper end of the EUV energy range and in the X-ray domain. Such a cross section scales with the energy as $\sigma(E) \propto E^{-\gamma}$ (Maloney et al. 1996), with $\gamma = 2.8$. As a consequence, photons with larger energies penetrate deeper into the atmosphere.

The zenith angle is chosen to be $\theta = 60^\circ$, considered a good approximation for the globally averaged profile (Johnstone et al. 2018). We set the total X-ray luminosity to $L_X = 1 \times 10^{28}$ erg s $^{-1}$, and we select the spectral shape corresponding to a plasma temperature $T_X = 0.5$ keV (see Locci et al. 2018). For the atmospheric temperature we use the fiducial value $T = 1000$ K, consistent with a planetary orbital distance $d_p = 0.045$ au. Finally, we do not include mass flux entering or leaving the system at the top and bottom boundaries.

All the assumptions reported above identify our reference model (hereafter RF model). In the following, we will present the molecular vertical distribution for the RF model. Next, we will compare them to those obtained varying some critical stellar and atmospheric parameters (see Table 2). Of particular interest are those quantities affecting directly the transfer of

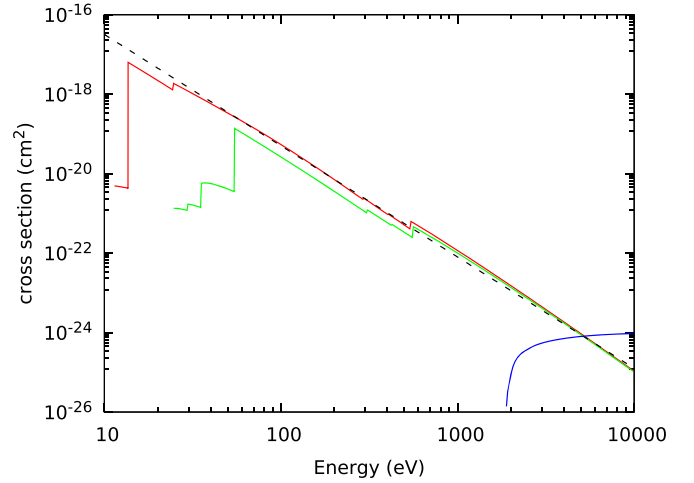


Figure 3. Total photoionization cross section (cm^2) as a function of the energy (eV) of the incoming photon. Red solid line: neutrals; green solid line: cations; blue solid line: Compton ionization cross section (Locci et al. 2018); black dashed line: straight-line approximation, $\sim E^{-2.8}$.

Table 2
Models and Model Parameters

Model	L_X ($\times 10^{28}$ erg s $^{-1}$)	T_X (keV)	EUV ^a (Y/N)	Z/Z_\odot	Notes
RF	1	0.5	Y	1	Reference (default)
LA	0.1	0.3			Low stellar activity
HA	100	1.0			High stellar activity
NX	0		Y		No X-rays
NE			N		No EUV radiation
UV	0		N		Just near and vacuum UV
NS					No secondary electrons
LM				0.1	Low metallicity
HM				10	High metallicity

Note.

^a EUV and X-ray luminosities are related through the empirical scaling law given in Sanz-Forcada et al. (2011); thus, a high X-ray luminosity corresponds to a high stellar activity in both the EUV and X-rays spectral bands.

high-energy photons within the atmosphere, i.e., the stellar activity and the metallicity. In order to understand the impact of different radiation energy ranges, we include some pathological unrealistic cases, e.g., suppressing the EUV spectral band or the effects of the secondary electron cascade.

3. Results

The ionization rate and the electron production, together with the rate of molecular dissociation (or dissociative ionization), are direct manifestations of the impact of the stellar energetic radiation on the atmospheric gas. We will describe the results proceeding from the top to the bottom of the atmosphere, i.e., for decreasing importance of photochemical effects. The top panel of Figure 4 shows that in the uppermost layers gas ionization is dominated by radiation in the UV range, through valence ionization of atomic carbon (11.3 eV), and in the EUV spectral band, mainly via H (13.6 eV) and He (24.6 eV) ionizations. In the upper atmospheric layers the ionization is largely primary, while deeper down in the atmosphere, $P \gtrsim 1 \times 10^{-8}$ bars, secondary

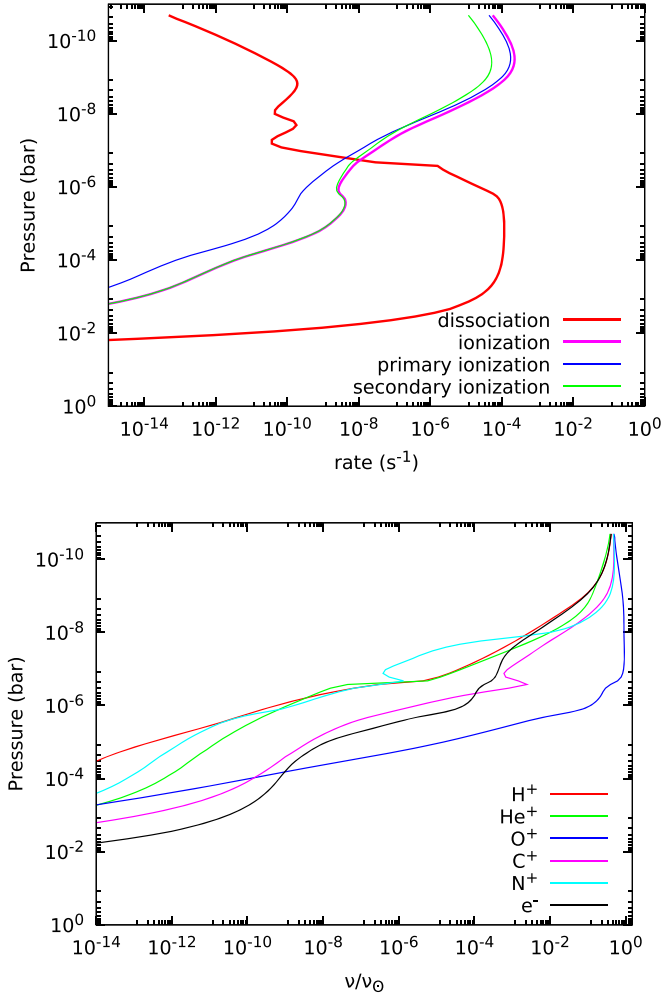


Figure 4. Photochemical rates, and ion and electron profiles in the RF model. Top panel: trends of different radiation-induced exit rates; bottom panel: vertical distribution of normalized volume mixing ratios of atomic ions and electrons.

ionization dominates, tracing the outbreak of X-rays. Although secondary ionization rates are lower than those produced by primary ionization, such residual ionization has a strong impact on molecular chemistry, which otherwise would be mostly driven by neutral–neutral reactions. This is a direct consequence of the much deeper penetration of X-ray radiation in atmospheres with solar-like composition. Photochemical effects decline significantly at pressures larger than $\sim 10^{-3}$ – 10^{-2} bars. The vertical plateau in the cumulative dissociation rate marks the appearance of molecular species, which follows the drop of ionization.

In the bottom panel of Figure 4 we show the vertical distribution of volume mixing ratios ν of atomic ions, normalized to the total concentrations of the corresponding elements, ν_{\odot} . In a totally ionized gas, all normalized ratios tend to $\nu/\nu_{\odot} = 0.5$, a value that includes the electron contribution. Also displayed in the bottom panel of Figure 4 is the electron concentration, which follows closely the proton profile at the lowest pressures. Increasing the pressure, going deeper into the atmosphere, oxygen is the major repository of the ionization, which is mainly induced by EUV radiation up to pressures $P \sim 10^{-7}$ when X-rays take over, ejecting core (and Auger) electrons from the K shells of C (0.28 keV), N (0.40 keV), and O (0.53 keV), spotted by the spikes (or bumps) in the C, N, and

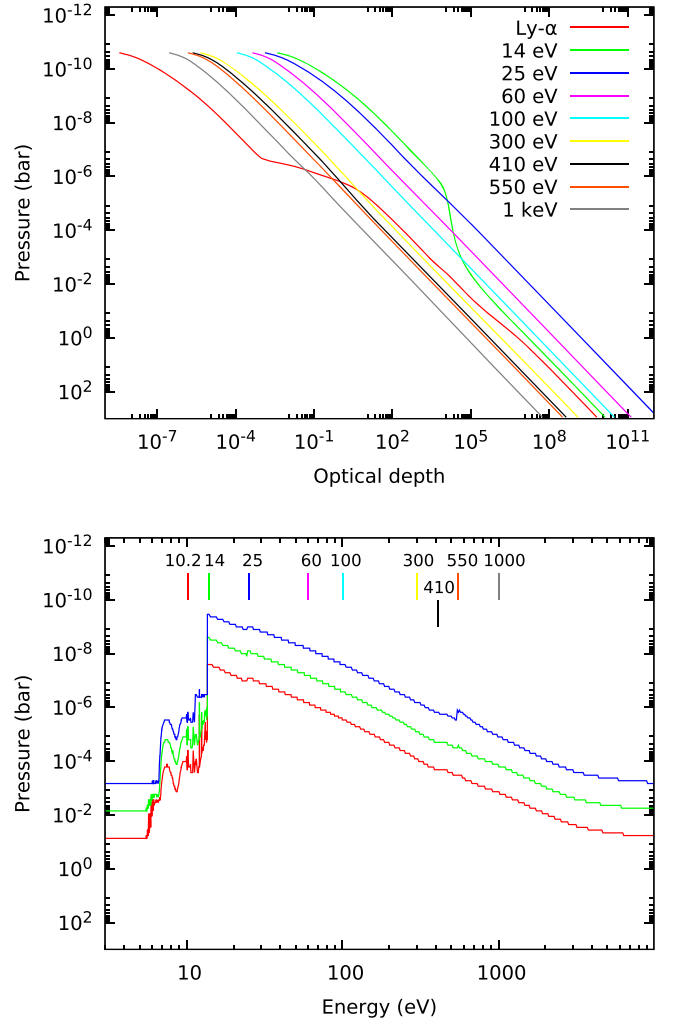


Figure 5. Optical depths of photons of different energies. Top panel: distribution along the vertical pressure profile; bottom panel: pressure level at which $\tau(E) = 1$ (blue line), 10 (green line), and 100 (red line). Labels indicate the set of photon energies (eV) exploited in the top panel.

O profiles at pressures around $P \sim 10^{-6}$ bars. This is confirmed by the onset of secondary ionization occurring approximately at the same altitudes (as shown in the top panel of Figure 4). Descending further, oxygen keeps controlling the ionization through molecular ions (see the next section), up to pressures $P \sim 10^{-3}$ – 10^{-2} bars, at which cloud formation should occur (Madhusudhan 2019). Such trends reflect the behavior of the ionization cross sections, with oxygen possessing the largest ones in both the EUV and X-ray bands.

3.1. The Spectral Distribution of Radiation within the Atmosphere

In the top panel of Figure 5 we show the resulting atmospheric optical depth at different photon energies. Being defined through Equation (5), the optical depth at a given energy is sensitive to the concentration of a chemical species and its ability to interact with radiation in that energy range. In the topmost layers, the Ly α line central frequency is optically thin. This line becomes thick ($\tau \gtrsim 1$) at $P \sim 5 \times 10^{-7}$ bars. When the pressure reaches the 10^{-5} bar level, the optical depth has increased by about 4 orders of magnitude, because of the rising densities of molecular species (see the upper plateau in

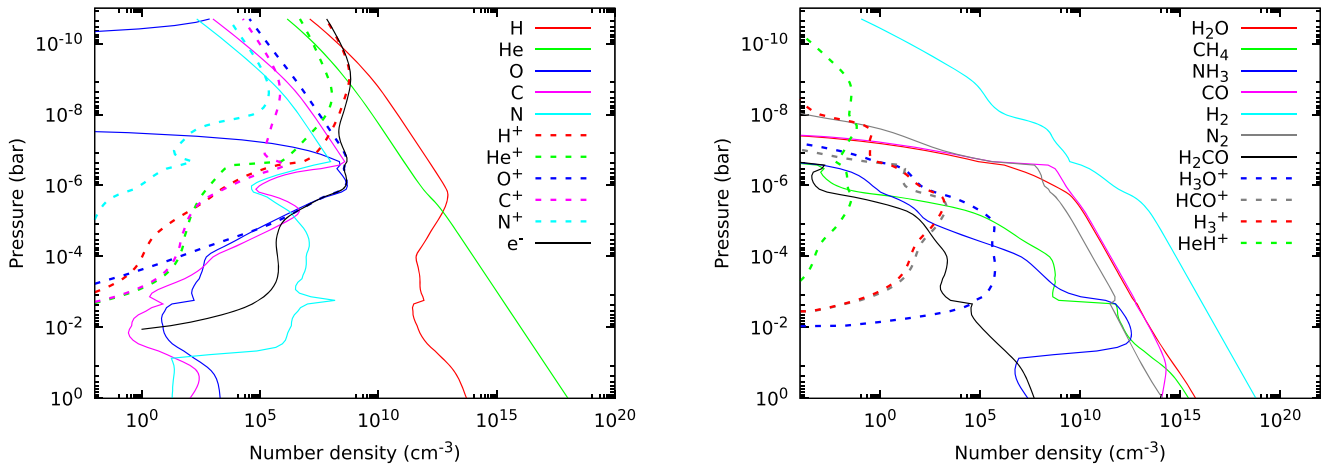


Figure 6. Atomic (left panel) and molecular (right panel) vertical number density profiles for a selected set of species under the conditions of the RF model.

Table 3
Ion/Neutral Pressure Crossing Points (Bars)

Atom	Model							
	RF	LA	HA	LM	HM	NX	NE ^a	NS
H	1.3(-10) ^b	2.0(-11)	1.8(-9)	1.6(-10)	1.3(-10)	1.3(-10)		1.3(-10)
He	8.9(-11)	2.0(-11)	3.1(-9)	1.6(-10)	8.9(-11)	8.9(-11)		8.9(-11)
C	6.9(-10)	1.4(-10)	5.4(-9)	5.5(-10)	7.0(-10)	6.9(-10)		6.9(-10)
N	8.5(-10)	2.1(-10)	6.7(-9)	8.4(-10)	8.6(-10)	8.5(-10)		8.5(-10)
O	8.3(-7)	8.3(-8)	1.3(-4)	1.7(-4)	3.4(-7)	6.5(-8)	2.0(-5)	2.0(-5)

Notes.

^a A blank space indicates that the ion concentration is lower than that of the corresponding neutral throughout the atmosphere.

^b 1.3(-10) = 1.3×10^{-10} .

the dissociation rates; top panel of Figure 4). From this location on, Ly α radiation is virtually extinct; see the bottom panel Figure 5, in which is shown the pressure at which a photon of a given energy reaches the apical value of $\tau=100$. Higher-energy photons (e.g., $E = 14$ eV, a value slightly larger than the energy threshold of atomic hydrogen ionization) present optical depths increasing rapidly up to pressures at which molecular species begin to form, $P \sim 10^{-5}$ bars. There, most of the hydrogen atoms are segregated in molecular compounds. We find that, in general, EUV radiation is totally removed starting from $P \gtrsim 10^{-6}$ bars. Higher-energy radiation is progressively damped with increasing pressure, but still capable of maintaining a chemically significant ionization level. Around $P \sim 10^{-4}$ bars, the gas (now predominantly molecular) is illuminated by X-rays with energies $E \gtrsim 300$ eV, which are able to penetrate quite easily through the atmospheric layers, reaching very low altitudes. As we already pointed out, since photoionization cross sections scale with a negative power of the energy, the photon penetration depth increases with the energy. However, in the energy range exploited in this work, photons do not penetrate much lower than 0.1–1 bars (depending on the illumination), where other phenomena (e.g., dynamics) may be dominant.

3.2. The Atomic and Molecular Distributions

The atmospheric gas-phase abundances for our RF model are presented in Figure 6, for a selected number of atomic or molecular species, in either neutral or ionized forms.

As evident from Figure 6 (left panel), recombination of atomic ions to neutrals occurs rather high in the atmosphere for

H and He, $P \lesssim 10^{-10}$ bars, while C and N follow at a bit higher pressures $P \lesssim 10^{-9}$ bars. Neutral oxygen reaches the concentration level of O⁺ much more in depth, $P \sim 10^{-6}$ bars, as the K-shell ionization rate declines. These transition regions depend on the physical and chemical conditions of the atmosphere, as reported in Table 3, in which we summarize the pressure crossing points between ions and neutrals for all the atoms present in the network. Together with the RF model, we report the crossing points for most of the models listed in Table 1. It is worthwhile to recall that in the NX model the EUV spectral band is present and identical to that of the RF model. The first evidence stemming from these results is that at the topmost altitudes ionizations are entirely driven by EUV radiation. In fact, no crossing point exists when EUV radiation is suppressed (NE model), and no deviations from the results of the RF model appear in the NX (no X-rays) and NS (no secondary effects) models. Oxygen is the exception, exhibiting a crossing point in the NE model, suggesting that although EUV radiation is still the dominant driver of primary ionization, X-rays begin to contribute (see the NX model). Moreover, secondary ionization appears to be rather effective (NS model).

These trends are due to the different photon penetration depths with higher-energy photons penetrating deeper into the atmosphere. Since the oxygen K-shell ionization threshold is located at larger energies than those of carbon ($\Delta E \sim 200$ eV) and nitrogen ($\Delta E \sim 100$ eV), ionization events are produced at lower altitudes, at which the EUV radiation has begun to be significantly damped. As X-rays are extremely sensitive to the presence of metals, variations in the metallicity may impact on

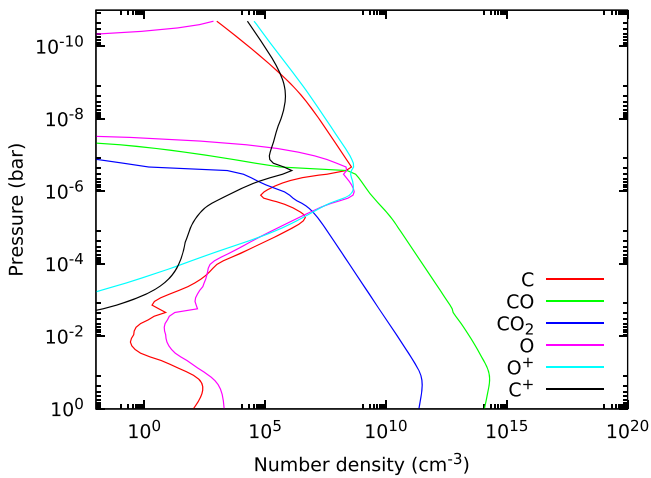


Figure 7. The $C^+/C/CO$ transition.

the atomic ions' distribution. We find that while C and N are scarcely affected, oxygen concentration responds quite appreciably to variations in the metallicity (LM and HM models). Increasing the stellar activity, both EUV and X-ray band fluxes increase (together with that of the Ly α). However, since their relation is almost linear, $\sim L_X^{0.86}$ (Sanz-Forcada et al. 2011), while the attenuation is exponential (see Equation (4)), the increase in the activity extends the region dominated by X-rays far beyond that in which EUV radiation matters. The net effect is an increase of the X-ray influence over the ionization (HA model). We also note that some elements (e.g., oxygen) may have additional deeper crossing points, due to the interplay of chemical reactions.

Recombination of hydrogen ends up in the formation of H_2 (the most abundant species), and at larger pressures also nitrogen becomes molecular. Once the concentration of O^+ declines, major repositories of oxygen are carbon monoxide and water. In a limited range of pressure ($P \sim 10^{-9}$ – 10^{-6} bars) the neutral carbon concentration encompasses all carbon nuclei, giving rise to a well-defined $C^+/C/CO$ transition (Figure 7), characteristic of interstellar photodissociation regions (e.g., Sternberg & Dalgarno 1995). In interstellar conditions (i.e., no radiation with energy higher than the Lyman continuum), however, neutral atomic carbon is typically underabundant. In gas subjected to high-energy photon irradiation, oxygen ionization is much more extended than that of carbon, and CO formation is delayed toward higher pressures, allowing the neutralization of carbon ions. At the same pressure level as CO, H_2O begins to form. Its formation rate is partially inhibited by the ionization content of the gas, while its destruction is mainly powered by UV radiation. Ammonia and methane increase their abundances deep in the atmosphere (Figure 6(b)), although in lower concentrations than CO and H_2O .

As secondary ionization starts to dominate the electronic content, i.e., when photochemistry is mainly driven by X-rays, heavy molecular ions begin to form. These species are less abundant than neutral species, reside at intermediate altitudes in the atmosphere ($P \sim 10^{-7}$ – 10^{-2} bars), and are mostly dependent on radiation chemistry. One of the most abundant is the hydronium ion, H_3O^+ , resulting from the protonation of water. The absence of H_2O^+ suggests an active proton-transfer chemistry, $H_3^+ + H_2O \rightarrow H_3O^+ + H_2$. H_3^+ depends on the electron content, as its formation occurs through $H_2 + H_2^+ \rightarrow H_3^+ + H$, and the dihydrogen cation, H_2^+ , is

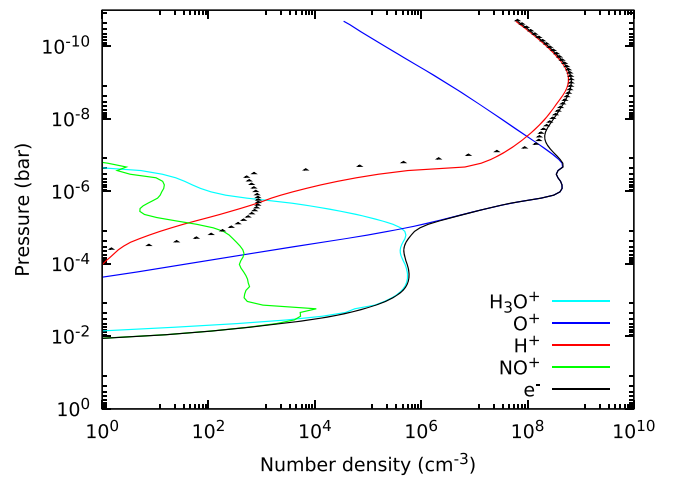


Figure 8. Vertical density profiles of electrons and their major contributors under the conditions of the RF model (solid lines). Black symbols indicate the distribution of the electron density suppressing X-rays (NX model).

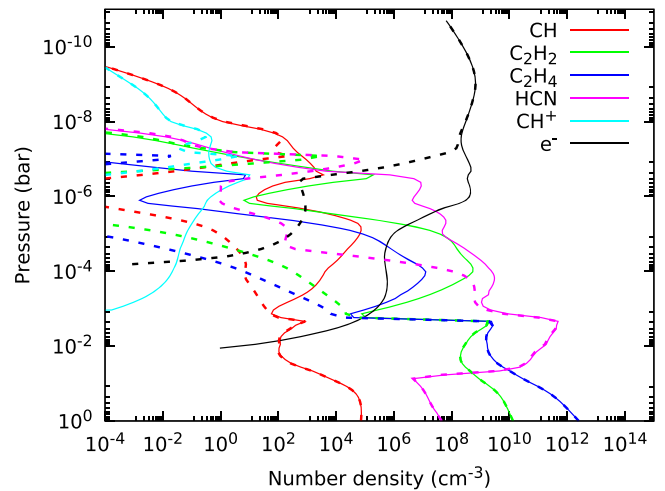


Figure 9. The vertical distribution of some C–H-bearing species including hydrogen cyanide (HCN) in the RF (solid line) and NX (dashed lines) models.

formed mainly by electron impact ionization of H_2 (15.4 eV), at altitudes where EUV radiation is suppressed. H_3^+ is a universal protonator, initiating a chain of ion–neutral reactions that is responsible for the formation of many molecular ions, such as HCO^+ , coming from protonation of CO.

In Figure 8 we report the major indicators of the gas electron content. As discussed in the previous section, with increasing pressures, first hydrogen and then oxygen are the dominant providers of electrons. At lower altitude, the abundance profile of the hydronium ion (together with other metal molecular ions, e.g., NH^+) appears to be tightly correlated with the electron distribution, for reasons related to the H_3O^+ formation channel (see the previous section).

The methylidyne radical (CH) and cation (CH^+) and the hydrocarbons acetylene (C_2H_2) and ethylene (C_2H_4) show relatively large densities. Hydrogen cyanide (HCN) is also abundant. The concentration profiles of these species are reported in Figure 9. All of these molecules are positively sensitive to X-ray radiation, without which their abundances would be basically confined toward the bottom of the atmosphere. Photochemistry boosts their abundances upward

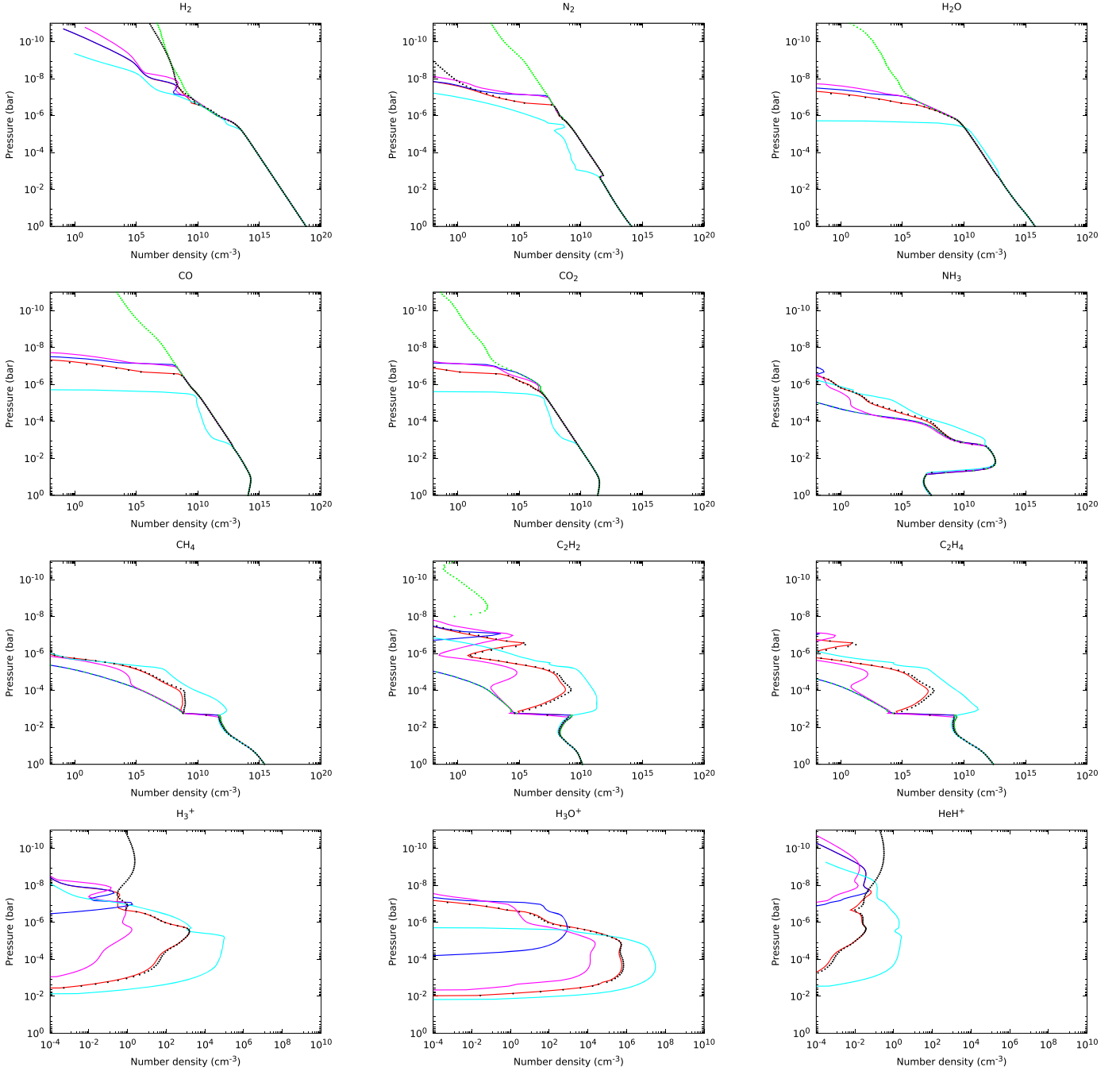


Figure 10. Atmospheric concentrations arising from different assumptions on the illuminating stellar high-energy flux. RF model ($L_X = 1 \times 10^{28} \text{ erg s}^{-1}$, $T_X = 0.5 \text{ keV}$): red lines; LA model ($L_X = 1 \times 10^{27} \text{ erg s}^{-1}$, $T_X = 0.3 \text{ keV}$): purple lines; HA model ($L_X = 1 \times 10^{30} \text{ erg s}^{-1}$, $T_X = 1 \text{ keV}$): pale blue lines; NX model (no X-rays): blue lines; UV model (no radiation with energy higher than the Lyman continuum): green symbols; NE model (no EUV radiation): black symbols.

at altitudes at which haze formation is expected, $P \sim 10^{-2}$ – 10^{-3} bars (Madhusudhan 2019).

3.3. Varying the Stellar Activity

As we have seen, chemistry may be sensitive to the effects of the different types of high-energy radiation. The characteristics of atmospheric chemical evolution emerge from many feedbacks on a wide range of timescales. Identifying and quantifying these processes is an essential step in the predictive outcome of our chemical modeling.

In Figure 10 we show the modifications in the abundances of a set of representative species, in response to different

assumptions on the intensity of the stellar ionizing radiation, i.e., in our context, the radiation of energy higher than the Lyman continuum. We find a clear separation in the response of molecular vertical profiles yielding two distinct trends, with some species having their abundances reduced by the increase in the stellar activity, while others have them enhanced. In the first group we find (among others) H_2 , N_2 , water, carbon monoxide, and CO_2 . We recall that we parameterize the stellar activity through the X-ray luminosity, which in turn determines the intensity in the EUV spectral band and $\text{Ly}\alpha$ line. Thus, it may happen that for some species the X-ray luminosity acts just as a tuning parameter, e.g., enhancing the EUV intensity, but

without effectively contributing to the chemistry. This is the case for molecular hydrogen, whose response to a different degree of stellar activity is driven entirely by EUV radiation, being practically insensitive to X-ray irradiation. This is easily understood on the base of the values assumed by the H_2 photoionization cross section ($\gamma \sim 3.2$) at the thresholds of EUV and X-ray spectral bands

$$\frac{\sigma_{\text{H}_2}(13.6 \text{ eV})}{\sigma_{\text{H}_2}(100 \text{ eV})} \sim \left(\frac{100}{13.6}\right)^{3.2} \sim 600. \quad (7)$$

However, deeper in the atmosphere, H_2 may present a residual ionization produced by collisions with the secondary electron cascade generated by X-rays.

The dependence of N_2 , water, and carbon monoxide and dioxide abundances on the X-ray flux is instead real, as traced by the overlapping of their vertical profiles in both the RF and NE models. While CO is scarcely affected by UV radiation (UV model), water and CO_2 (Venot et al. 2018) may be efficiently dissociated by UV radiation, in particular in the energy range close to the $\text{Ly}\alpha$ line because of its great relative intensity. This is evidenced by the fall of H_2O and CO_2 profiles for pressure lower than $\sim 10^{-6}$ bars in UV and NX models. Due to the larger concentration of O^+ , both water and carbon monoxide formation rates reduce with increasing ionization, and indeed they decline with increasing stellar activity; see the drop of CO and H_2O densities at pressures as large as $P \gtrsim 10^{-5}$ bars in the high-activity case (HA model). Moreover, the density profile of water does not show any change in the slope of its horizontal part, as compared to atmospheres with lower X-ray illuminations (LA and RF models). This means that the reduced water content is due to a shortage in reactants, rather than direct $\text{Ly}\alpha$ photodestruction. Even if in our model the $\text{Ly}\alpha$ intensity grows with the X-ray luminosity, the horizontal plateau in the abundance of water occurs at altitudes sufficiently low to make the UV radiation efficiently shielded (see Section 3.1). The CO formation rate is affected by X-rays similarly to water.

For the remaining neutral species and the molecular ions, the X-ray luminosity boosts their abundances as their formation channels increase with the electron content, or the products of dissociation. UV and EUV radiation play minor roles, as evidenced by the overlap of molecular profiles in the outcomes of NX and UV and the RF and NE models, respectively. Because of ionization, ammonia and methane benefit from additional sources of NH_2 and CH_3 , respectively. This occurs through chains of hydrogen abstraction, starting from NH^+ and CH^+ and ending up with the formation of NH_3^+ and CH_3^+ . At this stage, the chains are broken by electron dissociative recombination.

H_3^+ and HeH^+ show different trends in the upper atmospheric regions, where EUV radiation provides an additional exit channel through electron dissociative recombination. As already mentioned, H_2 electron impact ionization, whose rate increases with the X-ray luminosity, provides a significant source of H_2^+ and then H_3^+ ions. Other molecular ions benefit on some level from electron impact chemistry (see HA model).

3.4. The Role of Metallicity

Metallicity affects the chemistry in a relatively simple way, as molecular abundances scale with the mutual amount of the

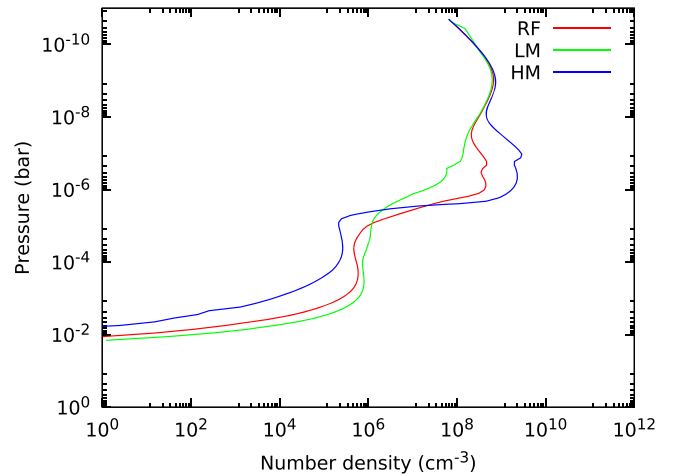


Figure 11. Metallicity-dependent electron density profiles in the atmosphere. RF model: red line; LM model: green line; HM model: blue line.

elements. However, since the gas photoionization cross section depends significantly on the presence and the concentrations of heavy elements, the degree of ionization is affected by variations in the elemental composition, yielding consequences in the molecular distribution.

In Figure 11 we report vertical profiles of the electron number density for three representative values of the metallicity, namely, the RF model, $Z/Z_\odot = 0.1$ (LM model), and $Z/Z_\odot = 10$ (HM model). The outer atmospheric layers do not show appreciable variations, as most of the electrons are provided by the photoionization of hydrogen. Since X-rays are more rapidly removed in the HM case, from $P \sim 10^{-8}$ bars down to $P \sim 10^{-5}$ bars the ionization initially increases with increasing metallicity, until the X-ray intensity declines appreciably, and the electron content falls sharply. The horizontal plateau in the electron density at $P \gtrsim 10^{-6}$ bars (RF and HM models) is, in fact, the response to the exponential decrease of the flux (see Equation (4)), while formation of H_3O^+ provides a new source of electrons that temporarily brakes the fall of the ionization content of the gas down to $P \sim 10^{-3}$ bars (see the next section). In the LM case, for opposite reasons, facilitated X-ray penetration favors the increase in the electron density at lower altitudes, making their vertical density profile much smoother.

Neutral species are affected at various degrees. For instance, the abundances of water are marginally perturbed, while CO and CO_2 may delay their formation up to a few orders of magnitude in a small range of pressures (Figure 12). While the fall in the water abundance is started by UV radiation (mainly $\text{Ly}\alpha$), the coincidence of the electron and CO densities, at the change of slope of the CO profiles, suggests that X-rays are responsible for CO removal. This simply reflects the decay of oxygen ionization due to X-rays, as is apparent by the overlapping of the profiles of O^+ and electrons (see Figure 8). In other words, increasing the altitude, CO is not destroyed, but stops to form efficiently. Since metallicity affects the penetration of ionizing radiation, the abundances of CO differentiate significantly in the three cases shown in Figure 12, due to the shift of the electron, and thus O^+ abundance profiles toward lower values ($P \sim 10^{-7}$ bars; see Figure 11).

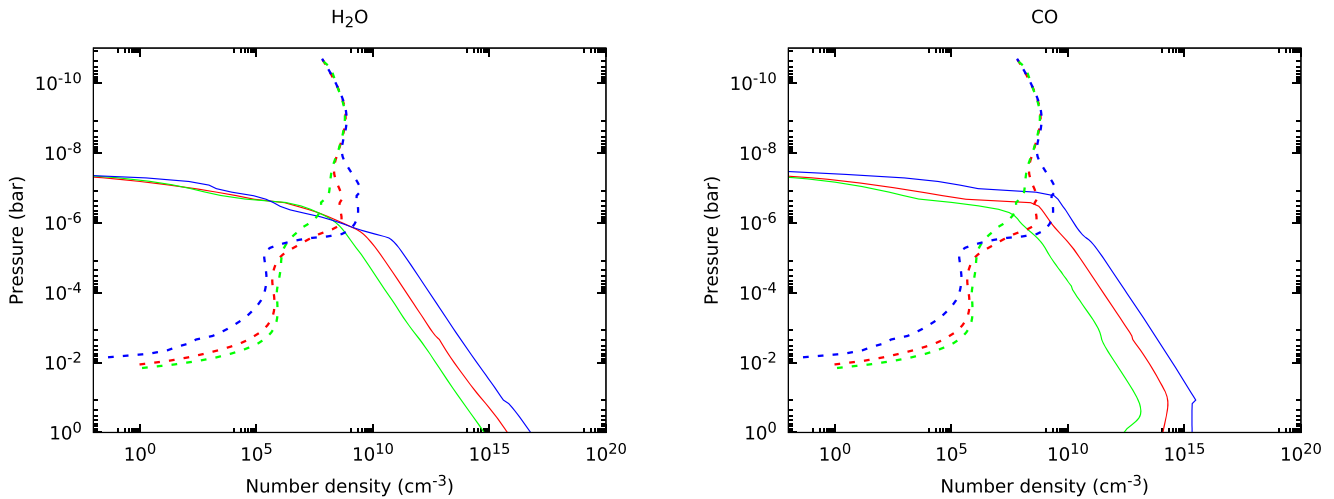


Figure 12. Water (left) and carbon monoxide (right) vertical profiles. LM model: green lines; RF model: red lines; HM model: blue lines. Dashed lines refer to the electron profiles; colors indicate the same models as in the case of molecular species.

4. Discussion and Conclusions

In this work we present an analysis of chemical processes induced by high-energy radiation, in a planetary atmosphere of solar-like composition. In particular, one of the major efforts in our investigation is the attempt to unfold the effects carried out by photons in different spectral bands. These effects frequently appear entangled and mixed by the interplay of chemical reactions, which provide a convolved response to radiation in the resulting molecular abundances. Such a quest is made even more difficult by the existing correlations among different portions of the stellar spectrum.

The spectral distribution of radiation within the atmosphere reflects the underlying photochemistry. While EUV radiation sets up the chemical (mainly atomic) distribution in the upper atmospheric layers, interacting predominantly with hydrogen- and helium-bearing species, its driving role tends to fade in favor of X-rays, more sensitive to the presence of heavy elements. We may place such a “boundary” at the location where carbon and oxygen are eventually bound into carbon monoxide molecules, i.e., at pressures (RF model) $P \sim 10^{-7}$ bars. Of course, no unique and sharp separation exists between EUV- and X-ray-dominated regions, and their mutual extent and overlapping depend on the elements involved, reaction rates, and the physical and boundary conditions.

The major conclusion of the present work is that X-rays are a fundamental ingredient in the chemistry of planetary atmospheres of gaseous giants. X-rays with their weak photoionization cross sections may push the gas ionization to pressures inaccessible to lower-energy radiation. Although X-rays interact preferentially with metals, the produced secondary electron cascade may collisionally ionize also hydrogen- and helium-bearing species, and this occurs at altitudes far below the ones UV and EUV photons may penetrate.

X-ray irradiation supplies molecular ions that give potentially observable signatures of the atmospheric ionization. A specific example is H_3O^+ , produced through protonation of the water molecules. The presence of abundant stable species inhibits routes involving hydrogen abstraction chains, such as the one related to the hydronium ion, initiated by the formation of the hydroxyl cation OH^+ , which can react with molecular hydrogen to form H_2O^+ and then H_3O^+ . As the major formation channel is $\text{H}_2\text{O} + \text{H}_3^+ \rightarrow \text{H}_3\text{O}^+ + \text{H}$, the abundance

of the hydronium ion is related to that of H_3^+ , which in turn depends on that of H_2^+ , produced by the electron impact ionization of H_2 . As a consequence, for each hydronium ion, one electron is produced. Since ionization of H_2 at those altitudes is the main source of electrons, this explains the tight correlation between the abundance profile of H_3O^+ and the electron concentration.

Chemical effects are not solely benign, as strong X-ray irradiation lowers appreciably the upper boundary of the residing regions of abundant species, such as water, CO, and CO_2 (from $P \sim 10^{-7}$ bars (RF model) to $\sim 10^{-5}$ bars (HA model)). At the same time, however, ammonia and methane increase their concentrations. The same occurs for hydrocarbons and HCN, which constitute the chemical base for photochemically generated hazes. Such hazes are of particular interest, as they may serve as a source of organic materials for potential chemical evolution of life on a planet (He et al. 2020). Although life is not certainly expected to originate in giant hot planets, this chemistry may provide information on the relevant reaction routes.






In conclusion, we have shown that stellar high-energy emission, in particular X-rays, may drive important changes in the mixing ratio profiles of atmospheric species. The strongest impact on the chemistry is expected in planets orbiting stars of young ages that have the highest level of chromospheric activity. However, as the lowest adopted value of X-ray luminosity $L_x = 1 \times 10^{27} \text{ erg s}^{-1}$ is typical of old stars (e.g., Schmitt & Liefke 2004), all the planets within a distance from the star $\lesssim 0.05 \text{ au}$ are affected by EUV and X-ray stellar radiation during their entire life.

Finally, we note that stars are variable in time, and they may be subjected to flares and other impulsive phenomena that increase their emissions for a limited amount of time. These periods of high activity may increase photochemical and ionization rates and thus impact atmospheric chemistry (e.g., Venot et al. 2016), and even provide persistence in the products of chemistry (Chen et al. 2021). The present analysis thus needs to be extended to erratic stellar emission.

We acknowledge contributions from ASI-INAF agreements 2021-5-HH.0 and 2018-16-HH.0. A.M. acknowledges partial support from PRIN INAF 2019 (HOT-ATMOS). We would

like to thank the anonymous referees for their comments that helped to improve the clarity of the manuscript.

ORCID iDs

Daniele Locci  <https://orcid.org/0000-0002-9824-2336>
 Antonino Petralia  <https://orcid.org/0000-0002-9882-1020>
 Giuseppina Micela  <https://orcid.org/0000-0002-9900-4751>
 Antonio Maggio  <https://orcid.org/0000-0001-5154-6108>
 Angela Ciaravella  <https://orcid.org/0000-0002-3127-8078>
 Cesare Cecchi-Pestellini  <https://orcid.org/0000-0001-7480-0324>

References

- Ádámkóvics, M., Glassgold, A. E., & Meijerink, R. 2011, *ApJ*, **736**, 143
 Agúndez, M., Parmentier, V., Venot, O., Hersant, F., & Selsis, F. 2014, *A&A*, **564**, A73
 Airapetian, V. S., Gloer, A., Gronoff, G., Hébrard, E., & Danchi, W. 2016, *NatGe*, **9**, 452
 Airapetian, V. S., Jackman, C. H., Mlynczak, M., Danchi, W., & Hunt, L. 2017, *NatSR*, **7**, 14141
 Arumainayagam, C. R., Herbst, E., Heays, A. N., et al. 2021, arXiv:2102.00094
 Asplund, M., Grevesse, N., Sauval, A. J., & Scott, P. 2009, *ARA&A*, **47**, 481
 Barth, P., Helling, C., Stüeken, E. E., et al. 2021, *MNRAS*, **502**, 6201
 Bourgalais, J., Carrasco, N., Changeat, Q., et al. 2020, *ApJ*, **895**, 77
 Cecchi-Pestellini, C., & Aiello, S. 1992, *MNRAS*, **258**, 125
 Cecchi-Pestellini, C., Ciaravella, A., & Micela, G. 2006, *A&A*, **458**, L13
 Cecchi-Pestellini, C., Ciaravella, A., Micela, G., & Penz, T. 2009, *A&A*, **496**, 863
 Chadney, J. M., Galand, M., Unruh, Y. C., Koskinen, T. T., & Sanz-Forcada, J. 2015, *Icar*, **250**, 357
 Chen, H., Zhan, Z., Youngblood, A., et al. 2021, *NatAs*, **5**, 298
 Dalgarno, A., Yan, M., & Liu, W. 1999, *ApJS*, **125**, 237
 Erkaev, N. V., Lammer, H., Odert, P., et al. 2013, *AsBio*, **13**, 1011
 Fontenla, J. M., Stancil, P. C., & Landi, E. 2015, *ApJ*, **809**, 157
 García Muñoz, A. 2007, *P&SS*, **55**, 1426
 Giacobbe, P., Brogi, M., Gandhi, S., et al. 2021, *Natur*, **592**, 205
 He, C., Hörst, S. M., Lewis, N. K., et al. 2020, *PSJ*, **1**, 51
 Helling, C., & Rimmer, P. B. 2019, *RSPTA*, **377**, 20180398
 Hudson, J. E., Vallance, C., & Harland, P. W. 2004, *JPhB*, **37**, 445
 Huebner, W. F., & Mukherjee, J. 2015, *P&SS*, **106**, 11
 Husser, T. O., Wende-von Berg, S., Dreizler, S., et al. 2013, *A&A*, **553**, A6
 Johnstone, C. P., Güdel, M., Lammer, H., & Kislyakova, K. G. 2018, *A&A*, **617**, A107
 King, G. W., Wheatley, P. J., Salz, M., et al. 2018, *MNRAS*, **478**, 1193
 Kitzmann, D., Heng, K., Rimmer, P. B., et al. 2018, *ApJ*, **863**, 183
 Koskinen, T. T., Lavvas, P., Harris, M. J., & Yelle, R. V. 2014, *RSPTA*, **372**, 20130089
 Linsky, J. L., Fontenla, J., & France, K. 2014, *ApJ*, **780**, 61
 Linsky, J. L., Wood, B. E., Youngblood, A., et al. 2020, *ApJ*, **902**, 3
 Locci, D., Cecchi-Pestellini, C., Micela, G., Ciaravella, A., & Aresu, G. 2018, *MNRAS*, **473**, 447
 Lorenzani, A., & Palla, F. 2001, in ASP Conf. Ser. 243, From Darkness to Light: Origin and Evolution of Young Stellar Clusters, ed. T. Montmerle & P. André (San Francisco, CA: ASP), 745
 Madhusudhan, N. 2019, *ARA&A*, **57**, 617
 Madhusudhan, N., Agúndez, M., Moses, J. I., & Hu, Y. 2016, *SSRv*, **205**, 285
 Maloney, P. R., Hollenbach, D. J., & Tielens, A. G. G. M. 1996, *ApJ*, **466**, 561
 Micela, G. 2002, in ASP Conf. Ser. 269, The Evolving Sun and its Influence on Planetary Environment, ed. B. Montesinos, A. Gimenez, & E. F. Guinan (San Francisco, CA: ASP), 107
 Molaverdikhani, K., Henning, T., & Mollière, P. 2019, *ApJ*, **883**, 194
 Moses, J. I., Visscher, C., Fortney, J. J., et al. 2011, *ApJ*, **737**, 15
 Raymond, J. C., & Smith, B. W. 1977, *ApJS*, **35**, 419
 Ribas, I., Guinan, E. F., Güdel, M., & Audard, M. 2005, *ApJ*, **622**, 680
 Sanz-Forcada, J., Micela, G., Ribas, I., et al. 2011, *A&A*, **532**, A6
 Schmitt, J. H. M. M., & Liefke, C. 2004, *A&A*, **417**, 651
 Shematovich, V. I., Ionov, D. E., & Lammer, H. 2014, *A&A*, **571**, A94
 Shulyak, D., Lara, L. M., Rengel, M., & Nèmec, N. E. 2020, *A&A*, **639**, A48
 Sternberg, A., & Dalgarno, A. 1995, *ApJS*, **99**, 565
 Tsiaras, A., Waldmann, I. P., Tinetti, G., Tennyson, J., & Yurchenko, S. N. 2019, *NatAs*, **3**, 1086
 Venot, O., & Agúndez, M. 2015, *ExA*, **40**, 469
 Venot, O., Bénilan, Y., Fray, N., et al. 2018, *A&A*, **609**, A34
 Venot, O., Rocchetto, M., Carl, S., Roshni Hashim, A., & Decin, L. 2016, *ApJ*, **830**, 77
 Verner, D. A., Ferland, G. J., Korista, K. T., & Yakovlev, D. G. 1996, *ApJ*, **465**, 487
 Wakelam, V., Loison, J. C., Herbst, E., et al. 2015, *ApJS*, **217**, 20
 Yan, M., & Dalgarno, A. 1997, *ApJ*, **481**, 296